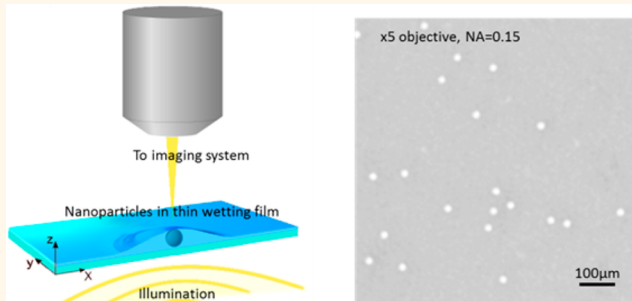


# Optical Detection and Sizing of Single Nanoparticles Using Continuous Wetting Films

Yves Hennequin,<sup>†</sup> Cédric P. Allier,<sup>†,\*</sup> Euan McLeod,<sup>§,⊥</sup> Onur Mudanyali,<sup>§,⊥</sup> Daniel Migliozzi,<sup>‡</sup> Aydogan Ozcan,<sup>§,⊥,||,¶</sup> and Jean-Marc Dinten<sup>†</sup>

<sup>†</sup>CEA, LETI, MINATEC, 17 rue des martyrs, 38054 Grenoble cedex 9, France, <sup>‡</sup>École Polytechnique (member of ParisTech), 91128 Palaiseau, France, and <sup>§</sup>Electrical Engineering Department, <sup>⊥</sup>Bioengineering Department, <sup>||</sup>California NanoSystems Institute, and <sup>¶</sup>Department of Surgery, David Geffen School of Medicine, University of California, Los Angeles, California 90095, United States

**ABSTRACT** The physical interaction between nanoscale objects and liquid interfaces can create unique optical properties, enhancing the signatures of the objects with subwavelength features. Here we show that the evaporation on a wetting substrate of a polymer solution containing submicrometer or nanoscale particles creates liquid microlenses that arise from the local deformations of the continuous wetting film. These microlenses have properties similar to axicon lenses that are known to create beams with a long depth of focus. This enhanced depth of focus allows detection of single nanoparticles using a low-magnification microscope objective lens, achieving a relatively wide field-of-view, while also lifting the constraints on precise focusing onto the object plane. Hence, by creating these liquid axicon lenses through spatial deformations of a continuous thin wetting film, we transfer the challenge of imaging individual nanoparticles to detecting the light focused by these lenses. As a proof of concept, we demonstrate the detection and sizing of single nanoparticles (100 and 200 nm), CpGV granuloviruses, as well as *Staphylococcus epidermidis* bacteria over a wide field-of-view of  $5.10 \times 3.75 \text{ mm}^2$  using a  $5\times$  objective lens with a numerical aperture of 0.15. In addition to conventional lens-based microscopy, this continuous wetting-film-based approach is also applicable to lens-free computational on-chip imaging, which can be used to detect single nanoparticles over a large field-of-view of  $>20-30 \text{ mm}^2$ . These results could be especially useful for high-throughput field analysis of nanoscale objects using compact and cost-effective microscope designs.



**KEYWORDS:** wetting films · optical microscopy · computational imaging · nanoparticle detection · virus detection · bacteria imaging

Imaging and microscopy have been experiencing a renaissance over the past decade, where a significant portion of these advances provides new nanoimaging capabilities. In particular, new label-free microscopy techniques are providing exciting paths to detect single nanoparticles down to 10 nm and viruses smaller than 100 nm in diameter.<sup>1–14</sup> These new optical tools can serve various applications in nanotechnology, including imaging of self-assembly processes at the nanoscale and the characterization of nanoparticle synthesis in terms of concentration, size, and aggregation. However, all these approaches are relatively low-throughput since they provide a limited imaging field-of-view (FOV), which is typically smaller than  $0.1-0.2 \text{ mm}^2$ . To improve

this limited FOV of lens-based imaging systems, here we present a thin wetting-film-based approach where a nanoparticle embedded in a *continuous* wetting film creates a microscopic axicon lens that is able to condense light along its optical axis over distances up to 3 orders of magnitude greater than the size of the particle itself. We characterize the optical properties of these axicon lenses and show that the shape and the condensing power of such liquid lenses can be fine-tuned to enable the detection of nanoparticles down to  $\sim 100 \text{ nm}$  using a low-magnification microscope objective, achieving a large FOV of several square millimeters. Note that these microscopic axicon lenses should not be confused with self-assembled

\* Address correspondence to cedric.allier@cea.fr.

Received for review April 17, 2013 and accepted July 26, 2013.

Published online July 27, 2013  
10.1021/nn403431y

© 2013 American Chemical Society

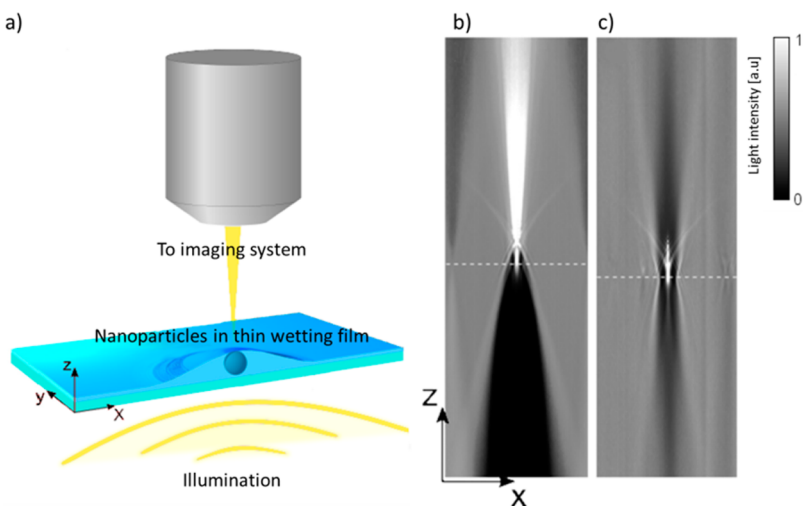


**Figure 1.** (a) Schematic of a liquid axicon lens consisting of a continuous liquid film wetting a microparticle (not to scale). The liquid lenses are formed by the evaporation of the water from aqueous suspensions containing dissolved polymer. This can be realized by simple drop evaporation on glass coverslips. The liquid lenses focus light primarily along the optical axis. (b) Microscopic image of the light cone produced by the liquid lens formed with a  $5\text{ }\mu\text{m}$  diameter particle and reconstructed from microscopic image stacks. The image dimension is  $15\text{ }\mu\text{m} \times 500\text{ }\mu\text{m}$ , and the dashed line indicates the position of the particle. (c) Same as in (b), but without the wetting film.

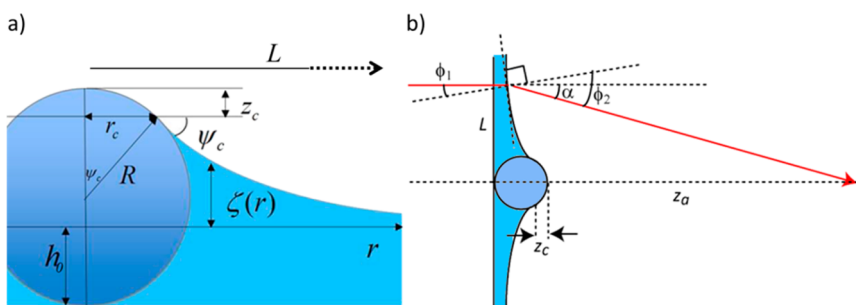


**Figure 2.** (a) Schematic representation of a particle in the polymer film spread on a flat substrate.  $R$  is the radius,  $h_0$  is the thickness of the film far away from the particle,  $z_c$  is the height of the spherical cap not covered by the liquid film,  $\zeta(r)$  is the height of the liquid meniscus, such that  $\lim_{r \rightarrow \infty} \zeta(r) = 0$ . (b) Schematic of how the liquid axicon lens refracts a normal-incidence ray (red).

isolated nanolenses that have been recently demonstrated for coherent detection of nanoparticles on a chip.<sup>15</sup> Here the physical origin is a local spatial deformations of a “continuous” wetting film rather than formation of “isolated” liquid refractive structures around each particle as in the case of nanolenses. Besides detection of nanoparticles using incoherent illumination and lens-based microscopy, we also demonstrate the simultaneous detection of single CpGV granuloviruses and *Staphylococcus epidermidis* bacteria over a wide field-of-view of  $5.10 \times 3.75\text{ mm}^2$  using a  $5\times$  objective lens that has a numerical aperture of 0.15. These microscale axicon lenses also enable the detection of single  $100\text{ nm}$  nanoparticles using computational lens-free imaging,<sup>15–25</sup> achieving an imaging FOV of  $>20\text{--}30\text{ mm}^2$ .

## RESULTS AND DISCUSSION

**Liquid Axicon Lenses.** When a small amount of buffer solution is deposited on a wetting surface, it spreads to form a flat drop that quickly evaporates, leaving

nonvolatile solutes on the substrate. With a polymer or concentrated surfactant solution, the evaporation of a microliter drop will leave a nearly flat film at the center of the drop bounded eventually with a thicker edge near the initial contact line.<sup>26</sup> Additionally, if particles are dispersed in the solution, they will be left as inclusions in the film, creating local spatial deformations of the interface provided their size is larger than the local film thickness. While the bulk of the film is totally transparent, these local deformations act as liquid axicon lenses that strongly condense light, providing a powerful means for detecting small particles.

First, the effect of the polymer film is demonstrated with relatively large  $5\text{ }\mu\text{m}$  particles. For this, we evaporate droplets of  $1\text{ }\mu\text{L}$  on a glass coverslip from two suspensions of beads with and without the dissolved polymer. We use conventional bright-field microscopy to make image stacks, focusing at successive depths in order to image the light cone produced by the beads (see Figure 1). The condensing power of the liquid lens formed by the bead under the polymer

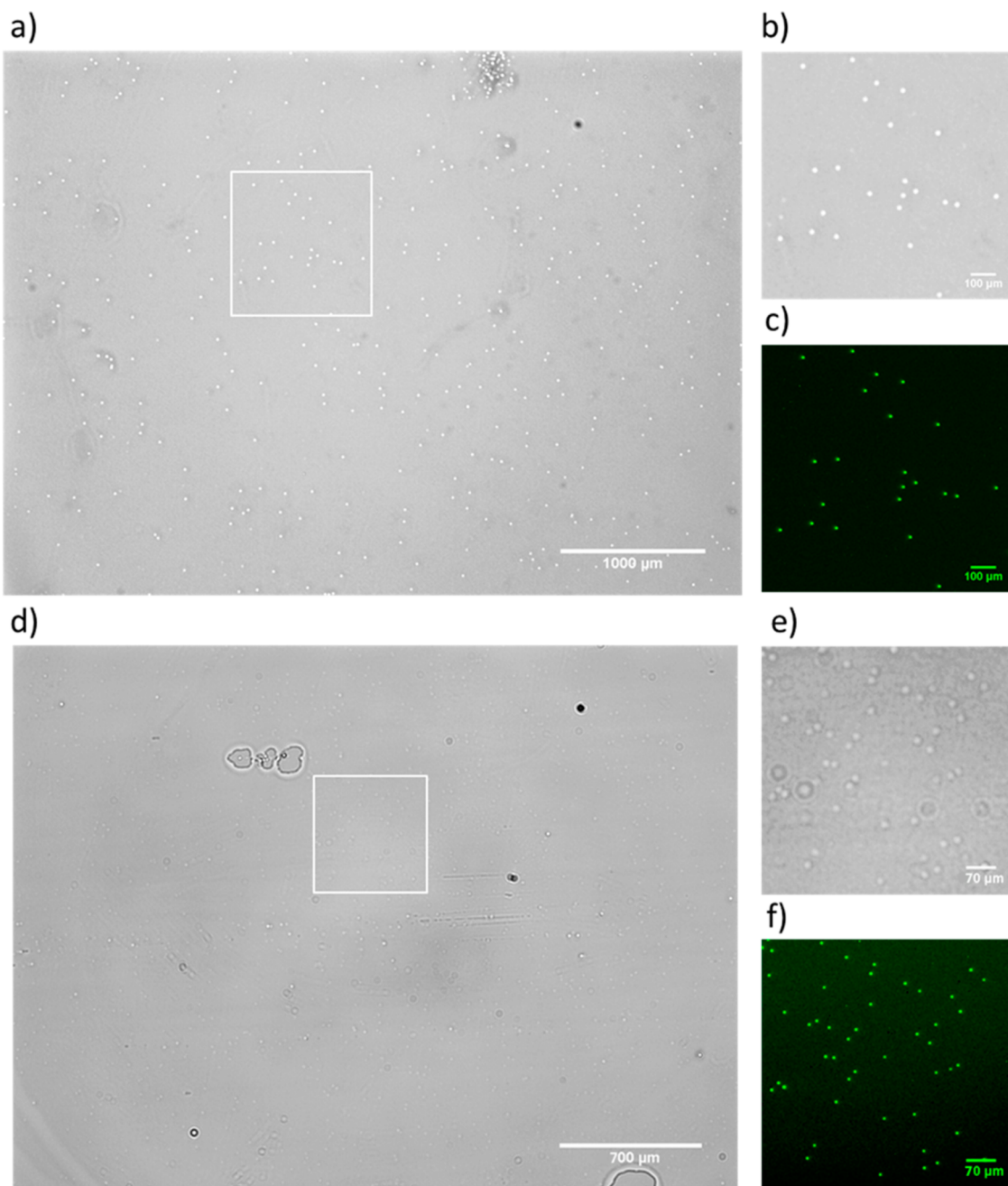


**Figure 3.** (a) Bright-field microscopic image of an evaporated drop with polymer (0.4% v/v PEG) and 200 nm particles taken at  $\sim 100 \mu\text{m}$  above the drop (5 $\times$  objective, NA = 0.15, 1.76 $\times$  effective magnification, FOV of 19.1 mm $^2$ ). Because of the liquid lenses formed by the polymer on top of the particles, the latter can be seen as white spots in the center of the drop despite the low magnification and large field-of-view (5.10 mm  $\times$  3.75 mm). (b) Close-up of the area indicated in (a). (c) Same area is shown under fluorescence microscopy. (d) Evaporated drop with polymer (0.2% v/v PEG) and 100 nm diameter particles (5 $\times$  objective, NA = 0.15, 2.5 $\times$  effective magnification, FOV of 9.4 mm $^2$ ). The white square has a side length of 0.66 mm, a close-up of which is shown in (e) in bright-field conditions and (f) in fluorescence.

film is evident: most of the light is focused on the optical axis, forming an almost nondiffracting beam, characteristic of an axicon lens (see Figure 1b). The direct consequence of this is that a significant contrast between the center of the interference pattern (local intensity maximum) and the image background persists up to distances of *millimeters* behind the liquid axicon lens. In contrast, a single bead without a polymer film focuses incoming light to a point at

relatively short distances (see Figure 1c). Beyond the focal point, the light cone rapidly expands while the on-axis intensity drops quickly to background level.

We can model and better understand these observations by computing the shape of the film with a spherical inclusion according to refs 27–29 (see Figure 2). Assuming complete wetting of a particle of diameter  $D$  by a film of thickness  $h_0$ , the local height  $\zeta(r)$  above  $h_0$  of the liquid meniscus around

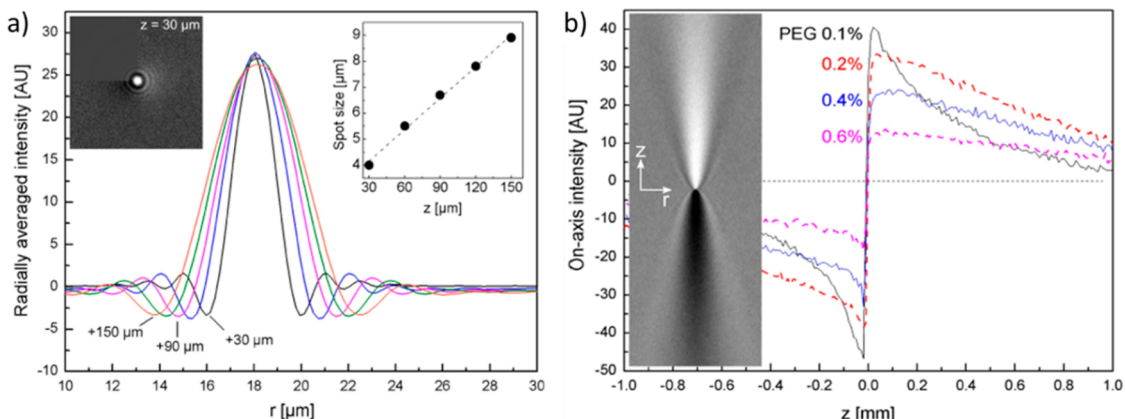


**Figure 4.** Optical characterization of the axicon liquid lenses that are formed by 200 nm particles in continuous PEG films. (a) Transverse intensity modulations at various focus depths. The curves are obtained by radially averaging the intensity from the center of the particle; see top-left quadrant in the upper-left inset, which shows the interference pattern produced 30  $\mu\text{m}$  above a 200 nm particle. The image width is 26  $\mu\text{m}$ . The central spot spreads linearly with the distance from the particle (upper-right inset). (b) On-axis intensity profiles for liquid lenses obtained by evaporating suspensions of varying PEG concentrations. The image shows the light cone reconstructed from 2D images of the liquid lens in (a). Image dimensions are 26  $\mu\text{m} \times 2000 \mu\text{m}$ .

the particle is a solution of the Young–Laplace equation (see Supporting Information):

$$\zeta(r) = -L \tan \Psi_c \frac{K_0\left(\frac{r}{L}\right)}{K_1\left(\frac{r_c}{L}\right)} \quad (1)$$

where  $L$  is the characteristic transverse length over which this liquid interface is distorted,<sup>28</sup>  $\Psi_c$  is the meniscus slope angle,  $r$  is the radial coordinate,  $r_c$  is the contact ring radius, and  $K_j$  is the  $j$ -th modified Bessel function of the second kind. For micrometer-thick films,  $L = (\gamma/\rho g)^{1/2}$  is the capillary length of the liquid which sets the size of the lens where  $\gamma$  is the film–air surface tension,  $\rho$  is the film density, and  $g$  is the gravitational acceleration.  $L$  is typically in the millimeter range for our experimental conditions. Near the particle (i.e., for  $r \ll L$ ), eq 1 can be approximated by<sup>29</sup>

$$\zeta(r) = -2z_c \left[ \ln\left(\frac{r}{2L}\right) + \gamma_e \right] \quad (2)$$

where  $z_c$  is the height of the spherical cap not covered by the liquid film and  $\gamma_e$  is the Euler–Mascheroni constant. The shape of the lens described in eq 2 is that of an *axicon* with a concave curved slanting side as discussed in ref 30. When illuminated with *coherent* light, an axicon lens forms an almost nonspread beam, focusing the light into a line along the optical axis over an extended distance.<sup>30–32</sup> On the other hand, in our lens-based experiments with *incoherent* light, the central spot is primarily formed through light concentration and refraction instead of coherent interference. From simple geometrical considerations, the maximal focal length  $z_a$  is determined by the convergence of the optical rays that start at the outer edges of the axicon lens (see Figure 2b):

$$z_a \approx \frac{L}{\tan(\alpha)} \approx \frac{L}{\phi_2 - \phi_1} \approx \frac{L}{(n - 1)\phi_1} \approx \frac{L}{(n - 1) \left| \frac{\partial \zeta}{\partial r} \right|_{r=L}} \approx \frac{L^2}{2(n - 1)z_c} \quad (3)$$

For our liquid axicon lenses,  $z_a$  can be nearly up to 3 orders of magnitude greater than the height of the microlens. In comparison, a single particle without the polymer film can only focus light at a distance approximately equal to its size, that is, on the order of micrometers<sup>33</sup> (see Figure 1c).

We now consider the case of nanoparticle detection. Here, thinner films are required to make a visible inclusion in the wetting film due to presence of nanoparticles. We note that for thinner wetting films, the main contribution to the capillary length  $L$  is now given by the disjoining pressure  $\Pi(h)$  in the film such that  $L = (\gamma/(\rho g - \Pi'))^{1/2}$ , where  $\Pi' = (d\Pi/dh)_{h_0}$ <sup>27</sup> (see Supporting Information). We assume that the disjoining pressure is determined by the van der Waals forces between the two interfaces of the film,  $\Pi(h) = A/6\pi h^3$ , with  $A$  being the Hamaker constant.<sup>34</sup> We find that, for a typical liquid polymer film on glass,  $L$  decreases sharply from millimeters to tens of micrometers for submicrometer film thicknesses. Therefore, despite the scaling down of its dimensions, local film deformations produced by nanoparticles should still focus light over relatively large distances, up to a few millimeters eventually. We managed to obtain thinner wetting films by lowering the polymer concentration, enabling the detection of single nanoparticles, that is, 200 and 100 nm diameter beads, while still using a low-magnification objective lens (see Figure 3, 5 $\times$  objective with NA = 0.15).

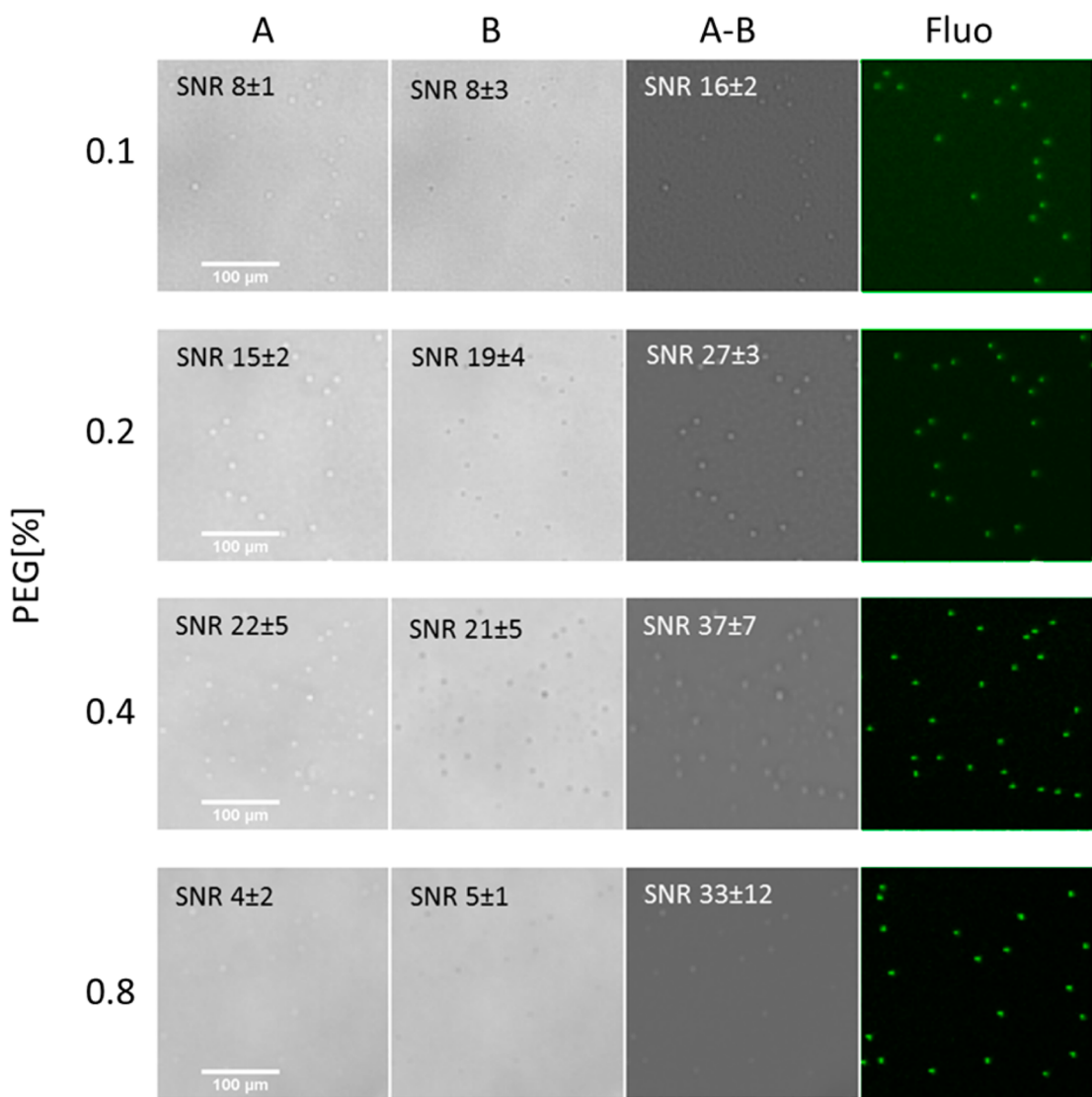


**Figure 5.** Microscope images (5× objective lens) focused at  $\sim 200\text{ }\mu\text{m}$  above (A) or below (B) the 200 nm particle plane for various PEG polymer concentrations. The signal-to-noise ratio is calculated as  $\text{SNR} = (I_{\text{max}} - \mu)/\sigma$ , where  $I_{\text{max}}$  is the local intensity maximum, and  $\mu$  and  $\sigma$  are the mean intensity and standard deviation of the intensity in a background noise region. The SNR almost doubles by subtracting the images focused above and below the particle plane, *i.e.*, (A,B).

In order to better characterize the liquid lenses, we also performed image stacks of the light intensity above and below the lens with higher magnification objectives (see Figure 4b, 50× objective, NA = 0.8). These characterization experiments once again confirmed that the light forms a slowly diverging cone with its shadow extending below the object plane. Figure 4 shows the influence of the polymer concentration on the optical properties of the liquid lenses. Surprisingly, for polymer concentrations greater than or equal to 0.2%, the on-axis intensity has a very consistent profile (see Figure 4b): it decreases almost linearly with the distance from the object. We note that these profiles are again similar to that of axicon-like lenses.<sup>31</sup> Remarkably, measured values of  $z_a$  are in the range of 1.3–2 mm. For instance, for  $D = 200\text{ nm}$

particles (see Figure 3a) and a polymer concentration of 0.2% v/v, we estimate  $z_a = 1.4\text{ mm}$  from the spread of the central spot. To detect even smaller particles, such as 50 nm particles, the film thickness would need to be reduced further; however, at low polymer concentrations required for such thin films, dewetting poses a significant challenge. As such, we cannot yet observe isolated 50 nm particles. At polymer concentrations of 0.1% v/v and lower, the depth of focus of the axicon lens reduces dramatically, even for larger particles (see Figure 4b). This suggests a transition to a different lens shape; in fact, the on-axis intensity profile now resembles that of a microdroplet (Figure 1c). This might be due to the partial dewetting of the film because nanometer-thin polymer films formed at low polymer concentrations become unstable.

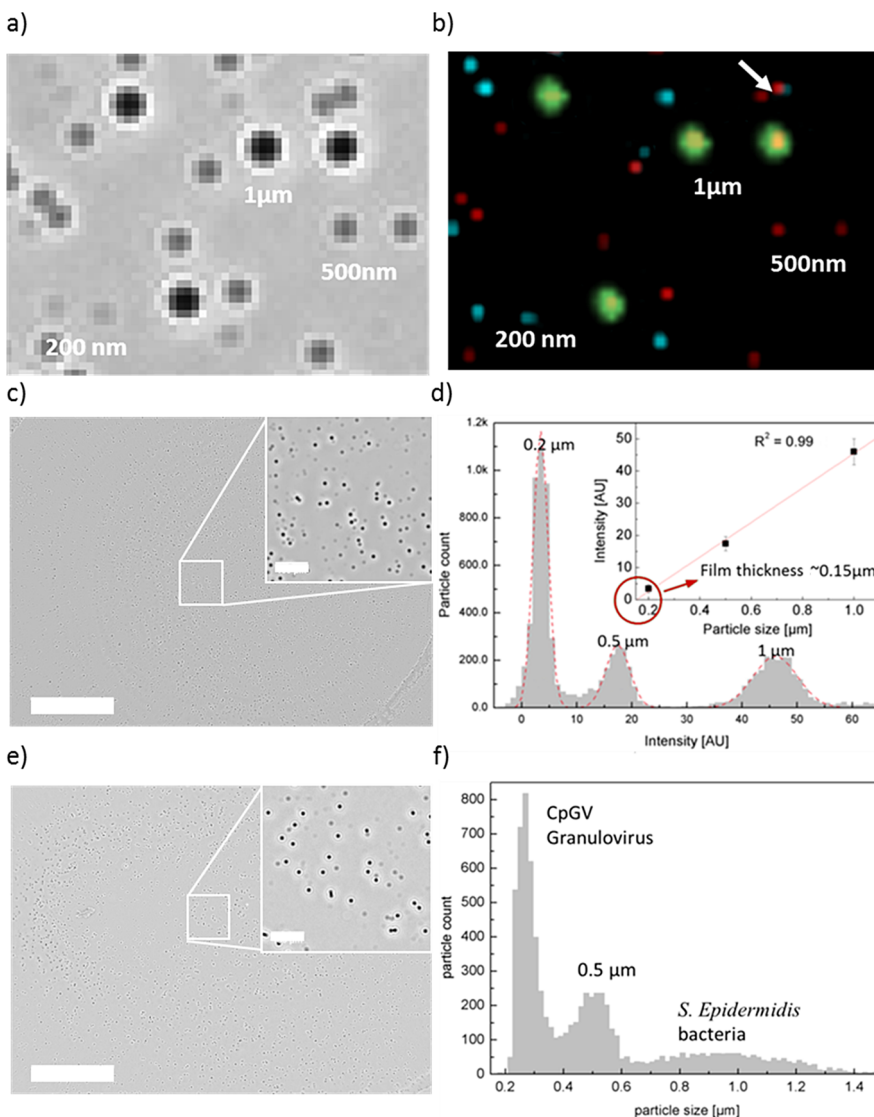


**Figure 6.** (a) Details of a  $19.1 \text{ mm}^2$  FOV bright-field microscopic image ( $5\times$  objective,  $\text{NA} = 0.15$ ) of an evaporated drop with continuous polymer thin film and 200 nm, 500 nm, and 1  $\mu\text{m}$  beads. For comparison purposes, the fluorescence microscopy image ( $5\times$  objective,  $\text{NA} = 0.15$ ) is shown in (b) with a color coding the different type of beads: 1  $\mu\text{m}$  in green, 500 nm in red, and 200 nm in blue. (c) Bright-field microscopic image ( $5\times$  objective,  $\text{NA} = 0.15$ ) of an evaporated drop with continuous polymer thin film and 200 nm, 500 nm, and 1  $\mu\text{m}$  beads. Scale bar is  $1000 \mu\text{m}$  ( $100 \mu\text{m}$  for the inset). (d) Local maxima intensity distribution measured on the image (c). The red curves show the Gaussian fits of the intensity peaks of the different particle patterns at 200 nm, 500 nm, and 1  $\mu\text{m}$  beads. The inner graph shows the plot of the local maxima intensity as a function of the particle diameters at 200 nm, 500 nm, and 1  $\mu\text{m}$ . The error bars represent the standard deviation of the local maxima intensity. (e) Bright-field microscopic image ( $5\times$  objective,  $\text{NA} = 0.15$ ) of an evaporated drop with continuous polymer thin film and CpGV,  $\sim 1 \mu\text{m}$  *Staphylococcus epidermidis* bacteria and 500 nm beads. Scale bar is  $1000 \mu\text{m}$  ( $100 \mu\text{m}$  for the inset). (f) Local maxima intensity distribution measured on the image (e). The inner plot in (d) serves as the calibration curve to plot the maxima distribution as a function of the particle size.

To preserve film stability at these low polymer concentrations, additional surface effects may need to be accounted for and the film stability can be better controlled by improving sample preparation steps, which will be a point of focus for future work. We should emphasize that the stability of the thin wetting film is important to enhance the signal-to-noise ratio (SNR) when detecting particularly small single nanoparticles. Although the absolute intensity may be greater at lower polymer concentrations (0.1–0.2%), the background noise is also larger, thus limiting

the SNR. The signal-to-noise ratio can be calculated as  $\text{SNR} = ((I_{\max} - \mu)/\sigma)$ , where  $I_{\max}$  is the local intensity maximum, and  $\mu$  and  $\sigma$  are the mean intensity and standard deviation of the intensity in a background noise region. Figure 5 shows the influence of the polymer concentration on the measured SNR with 200 nm beads ( $5\times$  objective lens). At higher polymer concentrations (e.g., 0.8%), the film is too thick and the condensing ability of the microlens is low. A coarse optimum is found at a PEG concentration of 0.4%, where the measured SNR is  $22 \pm 5$  (calculated for

$N = 25$  individual 200 nm particles). The SNR can be almost doubled to 37 by subtracting the image focused above and below the microlens, taking advantage of the asymmetric shadow cone observed in Figure 4b. Comparing the detection results from bright-field snapshots with those from fluorescence images, we find high detection efficiencies reaching  $\sim 90\%$ , with sample sizes on the order of  $10^3$  particles over a wide FOV of  $9.1 \text{ mm}^2$ .

**Particle Sizing Results.** Because the on-axis intensity depends on the film thickness relative to the particle diameter, the brightness of the central spot is consequently an indicator of the particle size. Measurements performed on mixed samples containing particle sizes of 0.2, 0.5, and 1  $\mu\text{m}$  show a linear relationship between intensity and particle size (see Figure 6). This method forms a simple way of sizing and evaluating different populations of objects within the same sample. As an example (see Figure 6f,g), we have probed a heterogeneous sample containing bacteria (*Staphylococcus epidermidis*) and viruses (CpGV granulovirus). On the basis of the size calibration curve (see Figure 6d inner graph), we can measure the granulovirus diameter to be  $330 \pm 50 \text{ nm}$  and the *Staphylococcus epidermidis* to be between 0.7 and 1.3  $\mu\text{m}$ . Indeed, the nominal size/diameter of *Staphylococcus epidermidis* is approximately 0.5–1.0  $\mu\text{m}$ .<sup>35</sup> Although the actual sizes of the granulovirus samples were not verified by SEM, the measured dimension are consistent with the literature values, that is, 200–450 nm in length.<sup>36</sup> These proof of concept experiments shows that it is possible to trap and detect different sizes of nanoparticles within the same polymer layer. However, when particles of different dimensions are too close to one another (distance  $< 10 \mu\text{m}$ ), the beads' signatures overlap due to the poor spatial resolution of the low NA objective lens, preventing the detection of the smallest bead. When the close particles are of equal dimensions, it is possible to resolve beads that are only 3.5  $\mu\text{m}$  apart (see white arrow in Figure 6a,b).

Note that all the experiments conducted in this work have been performed with spherical particles. In the case of nonspherical objects, such as various bacteria, we believe that similar contrast and depth of field related improvement factors as reported

in our article should be observed since the cross sections of various rod-shaped bacteria will still be circular and will possess similar refractive properties, at least for several diffraction planes. The 3D morphological differences due to nonspherical geometries of various objects would surely create modifications in the overall refractive behavior of the continuous wetting films, and these optical differences would be the subject of future analysis and experiments.

**Lens-Free On-Chip Imaging.** The collimation effect of the axicon liquid lenses can also be seen when focusing hundreds of micrometers away from the sample plane because the intensity decreases slowly with distance. Therefore, at the optimal polymer concentration (0.4%), we were also able to detect nanoparticles in a lens-free on-chip imaging setup (see Supporting Information).<sup>16–18</sup> In this setup, the imaging detector is a bare CMOS sensor (active area =  $6.12 \times 4.59 \text{ mm}^2$ ) without using imaging lenses. The distance between the coverslip and the sensor surface is on the order of  $500 \mu\text{m}$ . Without magnification, this lens-free imaging setup is able to detect single 100 nm particles across a very large field-of-view of  $\sim 28 \text{ mm}^2$  (see Figure S3). For each particle, the partially coherent diffraction pattern that is sampled at the detector plane has a fwhm of  $20 \mu\text{m}$  with an SNR of  $\sim 5$ .

## CONCLUSIONS

In summary we have described a simple, yet effective way of detecting nanoscale objects (e.g.,  $\sim 100$ –200 nm) over a large field-of-view. Creating spatial deformations on a continuous thin wetting film that behave as individual axicon lenses, nanoscale objects are detected using lens-based wide-field imaging configurations. The liquid axicon lenses have a high condensing ability along their optical axis, providing an opportunity for multiplexed detection of nanoscale particles and the estimation of their population levels within a liquid sample. This wetting-film-enabled detection of nano-objects across a wide field-of-view creates new opportunities, especially for opto-fluidic systems and may lead to new device concepts toward bringing nanoimaging capabilities to field settings and remote locations.

## METHODS

**Sample Preparation.** Samples are prepared by mixing aqueous stock solutions, polymer (PEG 600, Sigma-Aldrich), surfactant (Tween 20 or Pluronic F68 with  $C_s \sim 1 \text{ CMC}$ , Sigma-Aldrich), and particles (fluorescent carboxyl-modified latex beads, Sigma-Aldrich). Deionized water is always filtered through disposable syringe filters with a pore size of 0.2  $\mu\text{m}$ . The proportions of stock solutions are adjusted to reach the critical micelle concentration of the surfactant and a number of particles

of  $\sim 5 \times 10^3$  particles/ $\mu\text{L}$ . Microliter drops are simply placed on the cover glasses and left to evaporate at room temperature (20 °C). In order to form the wetting film, a microliter drop is deposited on a glass coverslip that was previously cleaned and rendered hydrophilic such that the contact angle of the drop is typically below 5°. Formation of the film proceeds by evaporation of the water: the contact line is first pinned after which an apparent contact line recedes while leaving a film of surfactant and polymer with the particles as inclusions.

**Substrate.** For the glass substrate, we use standard cover glasses (Corning) which are sonicated for approximately 10 min in a soap solution, then rinsed with deionized water, acetone, and isopropyl alcohol and dried with nitrogen. The cover glasses are subsequently placed for 30 s into oxygen plasma. This results in clean hydrophilic glass. Contact angles for water and polymer solutions are too low to be measured precisely but are below 5° (Kruss DSA100).

**Microscopy and Lens-Free on-Chip Imaging.** We observe the dried drops with bright-field and fluorescence microscopy (Olympus Provis AX70) with low-magnification objectives (5×, NA = 0.15 and 10×, NA = 0.3). To confirm that the revealed spots indeed correspond to the nanoparticles of interest, we used fluorescence microscopy to verify the locations of the particles against possible false positives from residual dust. In order to image the light cone, we make image stacks at high magnification (Zeiss AxioPlan, 50×, NA = 0.8). For lens-less imaging, we place the cover glass on a bare CMOS sensor (a 10MPixel 1/2.3 in. Aptina sensor) at a distance of 500 μm. The drop is illuminated with a red laser diode (650 nm, 3 mW) placed approximately 20 cm above the sensor. Intensity profiles are extracted using image analysis software (ImageJ, MatLAB). The on-axis intensity profile for each polymer concentration is computed by averaging the profiles of at least 10 microlenses.

**Conflict of Interest:** The authors declare the following competing financial interest(s): Aydogan Ozcan is the co-founder of a start-up company that aims to commercialize lens-free microscopy tools.

**Acknowledgment.** The work at CEA-Leti was supported by the Carnot Institutes Network. The authors thank L. Hervé and J.-G. Coutard for their support. Ozcan Research Group acknowledges the support of the Presidential Early Career Award for Scientists and Engineers (PECASE), ARO Young Investigator Award, NSF CAREER Award, ONR Young Investigator Award, and the NIH Director's New Innovator Award DP2OD006427 from the Office of The Director, NIH.

**Supporting Information Available:** Extended calculations of the shape of the liquid microlenses with corresponding figures. Contrast enhancement with a continuous wetting film and corresponding figures. Lens-free imaging of 100 nm particles with continuous thin wetting film and corresponding figures. Movie 1 shows in real-time the evaporation of a droplet with 200 nm particles as seen in a mixed bright-field and fluorescence microscopy (10×, NA = 0.3). Movie 2 shows in real-time a close-up on the moving evaporative front of a droplet with 200 nm particles as seen in bright-field microscopy. This material is available free of charge via the Internet at <http://pubs.acs.org>.

**Note Added after ASAP Publication:** This manuscript published ASAP on August 1, 2013. Figure 6 was replaced and the revised version was reposted on August 20, 2013.

## REFERENCES AND NOTES

1. Lindfors, K.; Kalkbrenner, T.; Stoller, P.; Sandoghdar, V. Detection and Spectroscopy of Gold Nanoparticles Using Supercontinuum White Light Confocal Microscopy. *Phys. Rev. Lett.* **2004**, *93*, 037401-1–037401-4.
2. Jacobsen, V.; Stoller, P.; Brunner, C.; Vogel, V.; Sandoghdar, V. Interferometric Optical Detection and Tracking of Very Small Gold Nanoparticles at a Water–Glass Interface. *Opt. Express* **2006**, *14*, 405–414.
3. Daaboul, G. G.; Yurt, A.; Zhang, X.; Hwang, G. M.; Goldberg, B. B.; Unlu, M. S. High-Throughput Detection and Sizing of Individual Low-Index Nanoparticles and Viruses for Pathogen Identification. *Nano Lett.* **2010**, *10*, 4727–4731.
4. Celebrano, M.; Kukura, P.; Renn, A.; Sandoghdar, V. Single-Molecule Imaging by Optical Absorption. *Nat. Photonics* **2011**, *5*, 95–98.
5. Wang, G.; Stender, A. S.; Sun, W.; Fang, N. Optical Imaging of Non-fluorescent Nanoparticle Probes in Live Cells. *Analyst* **2010**, *135*, 215–221.
6. Deutsch, B.; Beams, R.; Novotny, L. Nanoparticle Detection Using Dual-Phase Interferometry. *Appl. Opt.* **2010**, *49*, 4921–4925.
7. Kador, L.; Latychevskaia, T.; Renn, A.; Wild, U. Absorption Spectroscopy on Single Molecules in Solids. *J. Chem. Phys.* **1999**, *111*, 8755–8758.
8. Butter, J. Y. P.; Hecht, B.; Crenshaw, B. R.; Weder, C. Absorption and Fluorescence of Single Molecules. *J. Chem. Phys.* **2006**, *125*, 154710-1–154710-5.
9. Gerhardt, I.; Wrigge, G.; Bushev, P.; Zumofen, G.; Pfab, R.; Sandoghdar, V. Strong Extinction of a Laser Beam by a Single Molecule. *Phys. Rev. Lett.* **2007**, *98*, 033601-1–033601-5.
10. Tokeshi, M.; Uchida, M.; Hibara, A.; Sawada, T.; Kitamori, T. Determination of Suboctomole Amounts of Nonfluorescent Molecules Using a Thermal Lens Microscope: Subsingle Molecule Determination. *Anal. Chem.* **2001**, *73*, 2112–2116.
11. Gaiduk, A.; Yorulmaz, M.; Ruijgrok, P. V.; Orrit, M. Room-Temperature Detection of a Single Molecule's Absorption by Photothermal Contrast. *Science* **2010**, *330*, 353–356.
12. Wang, Z.; Guo, W.; Li, L.; Luk'yanchuk, B.; Khan, A.; Liu, Z.; Chen, Z.; Hong, M. Optical Virtual Imaging at 50 nm Lateral Resolution with a White-Light Nanoscope. *Nat. Commun.* **2011**, *2*, 1–13.
13. Szameit, A.; Shechtman, Y.; Osherovich, E.; Bullkitch, E.; Sidorenko, P.; Dana, H.; Steiner, S.; Kley, E. B.; Gazit, S.; Cohen-Hyams, T.; et al. Sparsity-Based Single-Shot Subwavelength Coherent Diffractive Imaging. *Nat. Mater.* **2012**, *11*, 455–459.
14. Wang, Z.; Millet, L.; Mir, M.; Ding, H.; Unarunotai, S.; Rogers, J.; Gillette, M. U.; Popescu, G. Spatial Light Interference Microscopy (SLIM). *Opt Express* **2011**, *19*, 1016–1026.
15. Mudanyali, O.; McLeod, E.; Luo, W.; Greenbaum, A.; Coskun, A. F.; Hennequin, Y.; Allier, C. P.; Ozcan, A. Wide-Field Optical Detection of Nano-Particles Using On-Chip Microscopy and Self-Assembled Nano-Lenses. *Nat. Photonics* **2013**, *7*, 247–254.
16. Repetto, L.; Piano, E.; Pontiggia, C. Lensless Digital Holographic Microscope with Light-Emitting Diode Illumination. *Opt. Lett.* **2004**, *29*, 1132–1134.
17. Mudanyali, O.; Tseng, D.; Oh, C.; Isikman, S. O.; Sencan, I.; Bishara, W.; Oztoprak, C.; Seo, S.; Khademhosseini, B.; Ozcan, A. Compact, Light-Weight and Cost-Effective Microscope Based on Lensless Incoherent Holography for Telemedicine Applications. *Lab Chip* **2010**, *10*, 1417–1428.
18. Isikman, S. O.; Sencan, I.; Mudanyali, O.; Bishara, W.; Oztoprak, C.; Ozcan, A. Color and Monochrome Lensless On-Chip Imaging of *Caenorhabditis elegans* over a Wide Field-of-View. *Lab Chip* **2010**, *10*, 1109–1112.
19. Allier, C. P.; Hennard, G.; Poher, V.; Dinten, J. M. Bacteria Detection with Thin Wetting Film Lensless Imaging. *Biomed. Opt. Express* **2010**, *1*, 762–770.
20. Allier, C. P.; Poher, V.; Coutard, J. G.; Hennard, G.; Dinten, J. M. Thin Wetting Film Lensless Imaging. *Proc. SPIE* **2011**, *8106*, 7906–7914.
21. Psaltis, D.; Quake, S. R.; Yang, C. Developing Optofluidic Technology through the Fusion of Microfluidics and Optics. *Nature* **2006**, *442*, 381–386.
22. Cui, X.; Lee, L. M.; Heng, X.; Zhong, W.; Sternberg, P. W.; Psaltis, D.; Yang, C. Lensless High-Resolution On-Chip Optofluidic Microscopes for *Caenorhabditis elegans* and Cell Imaging. *Proc. Natl. Acad. Sci. U.S.A.* **2008**, *105*, 10670–10675.
23. Schmidt, H.; Hawkins, A. R. The Photonic Integration of Non-solid Media Using Optofluidics. *Nat. Photonics* **2011**, *5*, 598–604.
24. Zheng, G.; Lee, S. A.; Yang, S.; Yang, C. Sub-pixel Resolving Optofluidic Microscope for On-Chip Cell Imaging. *Lab Chip* **2010**, *10*, 3125–3129.
25. Mudanyali, O.; Bishara, W.; Ozcan, A. Lensfree Super-Resolution Holographic Microscopy Using Wetting Films on a Chip. *Opt. Express* **2011**, *19*, 17378–17389.
26. Deegan, R. D.; Bakajin, O.; Dupont, T. F. Capillary Flow as the Cause of Ring Stains from Dried Liquid Drops. *Nature* **1997**, *389*, 827–829.

27. Kralchevsky, P. A.; Nagayama, K. Capillary Interactions between Particles Bound to Interfaces, Liquid Films and Biomembranes. *Adv. Colloid Interface Sci.* **2000**, *85*, 145–192.
28. Fiegel, J.; Jin, F.; Hanes, J.; Stebe, K. Wetting of a Particle in a Thin Film. *J. Colloid Interface Sci.* **2005**, *291*, 507–514.
29. Di Leonardo, R.; Saglimbeni, F.; Ruocco, G. Very-Long-Range Nature of Capillary Interactions in Liquid Films. *Phys. Rev. Lett.* **2008**, *100*, 106103-1–106103-4.
30. Lit, J. W. Y.; Tremblay, R. Focal Depth of a Transmitting Axiicon. *J. Opt. Soc. Am.* **1973**, *63*, 445–449.
31. McLeod, J. H. The Axiicon: A New Type of Optical Element. *J. Opt. Soc. Am.* **1954**, *44*, 592–597.
32. Durnin, J.; Miceli, J. J.; Eberly, J. H. Diffraction-Free Beams. *Phys. Rev. Lett.* **1987**, *58*, 1499–1501.
33. Born, M.; Wolf, E. Principles of Optics: Electromagnetic Theory of Propagation. *Interference and Diffraction of Light*; Cambridge University Press: London, 1997.
34. Israelachvili, J. N. *Intermolecular and Surface Forces*; Academic Press Inc.: New York, 1991.
35. Schleifer, K. H.; Kloos, W. E. Isolation and Characterization of *Staphylococci* from Human Skin I. Amended Descriptions of *Staphylococcus epidermidis* and *Staphylococcus saprophyticus* and Descriptions of Three New Species: *Staphylococcus cohnii*, *Staphylococcus haemolyticus*, and *Staphylococcus xylosus*. *Int. J. Syst. Evol. Microbiol.* **1975**, *25*, 50–61.
36. Capinera, J. *Encyclopedia of Entomology*; Springer: Berlin, 2008.